JOURNAL OF THE AMERICAN CHEMICAL SOCIETY

ARTICLE

pubs.acs.org/JACS

Magic Carbon Clusters in the Chemical Vapor Deposition Growth of Graphene

Qinghong Yuan,[†,∥] Junfeng Gao,[†,§,∥] Haibo Shu,[†,‡,∥] Jijun Zhao,[*,§] Xiaoshuang Chen,[*,‡] and Feng Ding[*,†]

[†]Institute of Textile and Clothing, Hong Kong Polytechnic University, Hong Kong, China

[‡]National Laboratory of Infrared Physics, Shanghai Institute for Technical Physics, Chinese Academy of Sciences, Yu Tian Road 500, Shanghai 200083, China

[§]Key Laboratory of Materials Modification by Laser, Ion and Electron Beams, Dalian University of Technology, Ministry of Education, Dalian 116024, China

Supporting Information

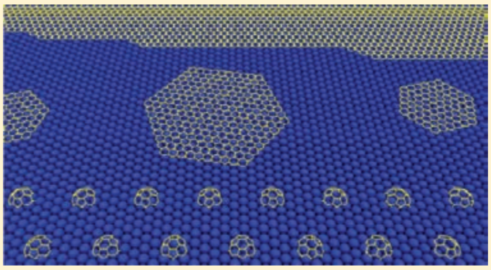

ABSTRACT: Ground-state structures of supported C clusters, C_N (N = 16, ..., 26), on four selected transition metal surfaces [Rh(111), Ru(0001), Ni(111), and Cu(111)] are systematically explored by ab initio calculations. It is found that the core−shell structured C_{21}, which is a fraction of C_{60} possessing three isolated pentagons and C_{3v} symmetry, is a very stable magic cluster on all these metal surfaces. Comparison with experimental scanning tunneling microscopy images, dI/dV curves, and cluster heights proves that C_{21} is the experimentally observed dominating C precursor in graphene chemical vapor deposition (CVD) growth. The exceptional stability of the C_{21} cluster is attributed to its high symmetry, core−shell geometry, and strong binding between edge C atoms and the metal surfaces. Besides, the high barrier of two C_{21} clusters' dimerization explains its temperature-dependent behavior in graphene CVD growth.

1. INTRODUCTION

Synthesizing high-quality graphene on a large scale is a great challenge for realizing graphene's various potential applications.[1−4] Among numerous methods of graphene synthesis, transition metal (TM) -catalyzed chemical vapor deposition (CVD) draws overwhelming interest because of the advantages of relatively low experimental temperature, easy transfer to various substrates, many adjustable experimental parameters, and the potential of synthesizing very high quality graphene with a very large area.[5] Various transition metals, for example, Ru,[6,7] Rh,[8] Ir,[9,10] Ni,[11,12] Pt,[13,14] Pd,[15] and Cu,[16,17] have been used as catalysts in graphene CVD growth. Despite the numerous experimental[3−15] and theoretical[18−24] investigations, knowledge for guiding experimental design is still very limited because of the lack of deep insight into the growth mechanism.

Facilitated with high-resolution microscopy technologies, detailed information on graphene CVD growth can be revealed.[7,9,25−27] One striking experimental finding is that uniform graphene clusters, whose diameter is ∼1 nm, were observed during the growth of graphene on Ru(0001),[26] Rh(111),[25] and Ir(111)[10] surfaces. They are the dominating C species in the initial stage of graphene growth at relatively low temperature, and then their fusion at high temperature initiates graphene nucleation. Very recently, similar behavior was observed in graphene growth on Ru(0001) surface with C_{60} as C feedstock.[27]

In previous reports, these dominant clusters were expected to be of similar size to C_{24}, which is composed of seven 6-membered-rings (7-6MRs).[25,26] But simulated scanning tunneling microscopy (STM) images of the 7-6MRs C_{24} are different from experimental ones.[25] Are these observed dominant C clusters the 7-6MRs such as C_{24}, or is there another type of C cluster that fits the experimental images better? How do these magic clusters dominate graphene growth at different temperatures? Does the existence of magic clusters depend on the type of metal catalyst? In order to answer these questions, we perform a systematic ab initio exploration on various potential structures of C_N (N = 16−26) clusters supported on four well-established catalyst surfaces: Rh(111),[8] Ru(0001),[6,7] Ni(111),[11,12] and Cu(111).[17,19] Our study reveals a surprising finding that a core−shell-structured C_{21} cluster consisting of three isolated pentagons with C_{3v} symmetry is notably stable on all four explored metal surfaces. Careful comparison of the experimental STM images, dI/dV curves, and cluster heights[25−27] with the simulated ones proves that C_{21} is the experimentally observed dominating C precursor. Further investigation shows that there is a significant barrier preventing the coalescence of C_{21} clusters. The magic cluster formation and the large barrier to their coalescence explain their temperature-dependent behavior in graphene CVD growth.

2. COMPUTATIONAL DETAILS

In this study, two types of slab models were used to represent the metal surfaces that interact with carbon clusters (C_N) and

Received: June 2, 2011
Published: November 12, 2011

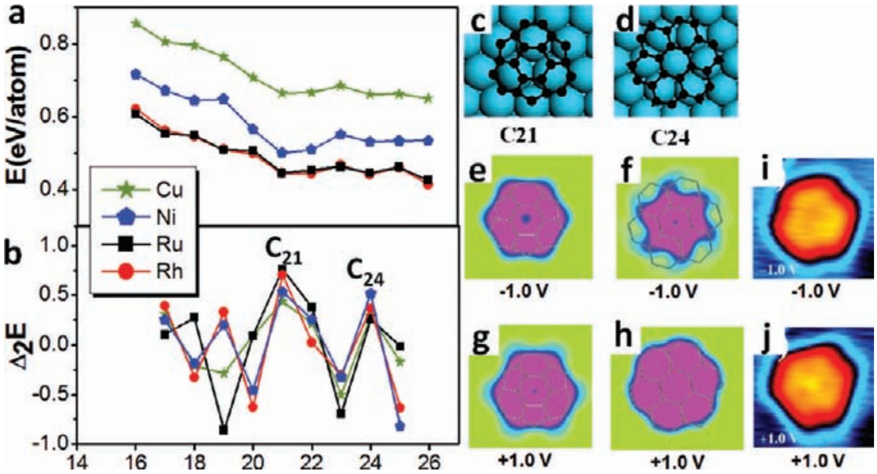

Figure 1. (a) Formation energies in electronvolts per atom and (b) their second derivatives, which are defined as $\Delta_2E = 0.5[E(N + 1) + E(N - 1)] - E(N)$, of the ground-state structures of supported C clusters on four catalyst surfaces: Ni(111), Cu(111), Ru(0001), and Rh(111). Magic-sized (c) C_{21} and (d) C_{24} on Rh(111) surface and their simulated STM images (e−h) at the voltages of +1.0 and −1.0 V, respectively, are shown. (i, j) Experimental STM images of the dominating C clusters observed in graphene CVD growth on Rh(111) surface are also shown for comparison.[25]

graphene nanoribbons (GNR), respectively. For carbon clusters C_N ($N = 16-26$) on metal surfaces [Rh(111), Ru(0001), Ni(111), and Cu(111)], a three-layer-thick metal slab with the bottom layer fixed was used to represent the metal surface. A four-layer slab model with fixed bottom layer was also used for the testing of a few configurations, and calculation results demonstrate that the three-layer slab model is accurate enough. The supercell of the slab model is composed of 6 × 6 repeating unit cells and the *k*-point mesh used for the calculation is 2 × 2 × 1. For every C_N, about 10 different configurations are optimized and the lowest one is taken as the ground-state structure (see ref 19 for details). Take C_{21} as an example, as shown in Figure S1 of Supporting Information: eight isomers are considered. For the calculation of GNRs (including armchair GNRs/AC-GNRs and zigzag GNRs/ZZ-GNRs) on metal surfaces, different supercells were used in order to match the lattice between GNR and metal surface. Cu(111) and Ni(111) surfaces have similar lattice parameters with that of GNR, thus the selected cell size for ZZ-GNR on Cu(111) and Ni(111) surfaces is $2.53 \times 21.85 \times 20$ Å^3, and cell size for AC-GNR is $4.37 \times 12.63 \times 20.0$ Å^3, and the corresponding *k*-point meshes are 5 × 1 × 1 and 3 × 1 × 1 respectively. For ZZ-GNR on Rh(111) and Ru(0001) surfaces, the selected cell size is $4.80 \times 16.00 \times 20.00$ Å^3 and the *k*-point mesh is 4 × 1 × 1. However, for AC-GNR on Rh(111) and Ru(0001) surfaces, a larger supercell with size of $14.00 \times 16.50 \times 20.00$ Å^3 was selected and only Γ point was used.

All calculations were carried out by a density-functional theory (DFT) method implemented in the Vienna ab initio simulation package (VASP).[28,29] The ion−electron interactions are treated with the projected augmented wave (PAW) pseudopotentials,[30] and the general gradient approximation (GGA) parametrized by Perdew, Burke, and Ernzerhof (PBE)[31] was used as exchange−correlation functional. All structures were optimized by a conjugate gradient method until the force component on every atom was less than 0.02 eV/Å. The kinetic energy cutoff was chosen as 400 eV. A climbing-image nudged elastic band (cNEB) method was employed to locate the transition states involved in the dimerization of two C_{21}s.[32] Non-spin-polarized DFT was used in all calculations except for special explanations in the main text. STM images were calculated within the Tersoff−Hamman approximation.[33]

3. RESULTS AND DISCUSSION

Various potential structures of C_N clusters in the size range $N = 16-26$ on four different metal surfaces are systematically explored with ab initio methods. The ground-state structures are shown in Figure S2 in the Supporting Information and the formation energies, which are defined as the energies of supported clusters relative to the energies of free-standing graphene, are shown in Figure 1a. On each of the four metal surfaces, a prominent valley around $N = 21$ is seen. The second derivatives of the formation energies (Figure 1b) clearly point out the magic size effect, that is, C_{21} is the maximum of the $\Delta_2E(N)$ curves on all four metal surfaces.[34] The ground-state structure of C_{21} on Rh(111) surface [named C_{21}@Rh(111)] is shown in Figure 1c. It has a core−shell structure with one hexagon in the center and three pentagons around, isolated by three hexagons. With the substrate symmetry taken into account, the C_{21}@Rh(111) has C_{3v} symmetry.

Similarly, C_{24} also can be identified as a magic cluster in the $\Delta_2E(N)$ curves. The 7-6MRs C_{24}@Rh(111) rotates ∼15° from the high-symmetry orientation during the structure optimization (Figure 1d) and therefore it has a relatively lower C_3 symmetry. The C_{24} and C_{21} clusters have very similar formation energies. The formation energies of C_{21}/C_{24} on Rh(111) and Ru(0001) surfaces are 0.444/0.442 and 0.445/0.446 eV, respectively. So, which one is the experimentally observed dominating graphene cluster?

In ref 25, Wang et al. proposed that these dominating carbon clusters must have lower formation energy than any smaller clusters or

$$E_N < E_i \qquad i = 1, 2, 3, ..., N - 1 \tag{1}$$

On Rh(111) surface, isolated C monomer has significantly lower formation energy and thus should be the main species of graphene growth.[35] Their calculation indicated that C_{24} is the smallest hexagonal carbon cluster that meets their criterion (1). Here, considering that the dominating cluster must stop growing at a certain size, we propose another criterion that *the next one greater than it must have higher formation energy* or

$$E_N < E_{N+1} \tag{2}$$

One can see from Figure 1 that both C_{21} and C_{24} on Rh and Ru surfaces meet criteria 1 and 2. While, on the way the carbon cluster grows larger, certainly *the smaller one, C_{21}, has higher priority of being formed first.*

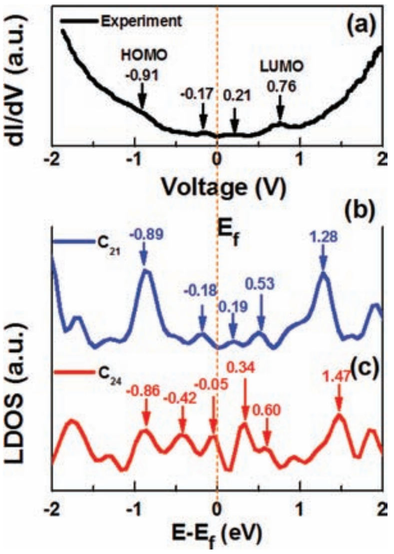

Figure 2. (a) Experimental d*I*/d*V* curve (extracted from ref 24) and local density of states (LDOS) of (b) C_{21} and (c) C_{24} on Rh(111) surface.

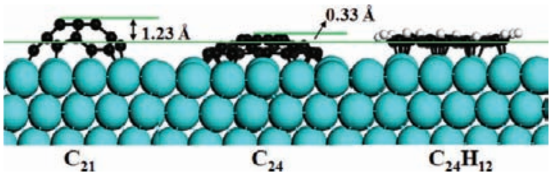

Figure 3. Heights of C_{21} and C_{24} on Rh(111) surface relative to coronene ($C_{24}H_{12}$) on Rh(111) surface.

To verify the experimentally observed dominating C clusters, STM images of C_{21} and 7-6MRs C_{24} on Rh(111) surface at voltages of +1.0 and −1.0 V are simulated. Both images of C_{21} have C_{3v} symmetry (Figure 1e,g) and are in good agreement with the experimental ones (Figure 1i,j).[25] On the contrary, the simulated STM images of C_{24}, which has rough C_6 symmetry at −1.0 V (Figure 1f) and rough C_{6v} symmetry at +1.0 V (Figure 1h), are rather different from the experimental ones.[25] The formation energies (E_f) and their second derivatives ($\Delta_2 E$) of C_N@Ru(0001) show nearly identical behaviors as those of C_N@Rh(111). The STM images of C_{21}@Ru(0001) and C_{24}@Ru(0001) are shown in Figure S3 of Supporting Information. Similarly, we can see that these simulated STM images of C_{21}@Ru(0001) are in good agreement with the experimental ones, which are shown in refs 26 and 27.

Beyond the comparison of STM images, more evidence that the experimentally observed dominating carbon clusters are C_{21} but not C_{24} can be identified. The calculated local density of states (LDOS) of C_{21} is in good agreement with the experimentally measured d*I*/d*V* curve, as shown in Figure 2.[25] As can be seen, three of the four peaks in the d*I*/d*V* curve between highest occupied and lowest unoccupied molecular orbitals (HOMO and LUMO) (Figure 2a) can be well-fitted by the LDOS curve of C_{21} (Figure 2b). The deviation of the LUMO peak from 0.76 to 0.53 is a consequence of DFT calculations normally underestimating the band gap. In sharp contrast, the LDOS of C_{24} has five peaks between the HOMO and LUMO and it is very difficult to figure out their corresponding positions in the d*I*/d*V* curve.

Moreover, the heights of optimized C_{21} and C_{24} on Rh(111) surface relative to that of coronene on Rh(111) surface have been calculated. The calculated results indicated that the highly curved C_{21} is ~1.2 Å higher than the coronene, while the C_{24} is only about 0.3 Å higher (shown in Figure 3). Apparently, the relative height of C_{21} fits the experimental measurement that the magic cluster is ~1 Å higher than coronene.[24]

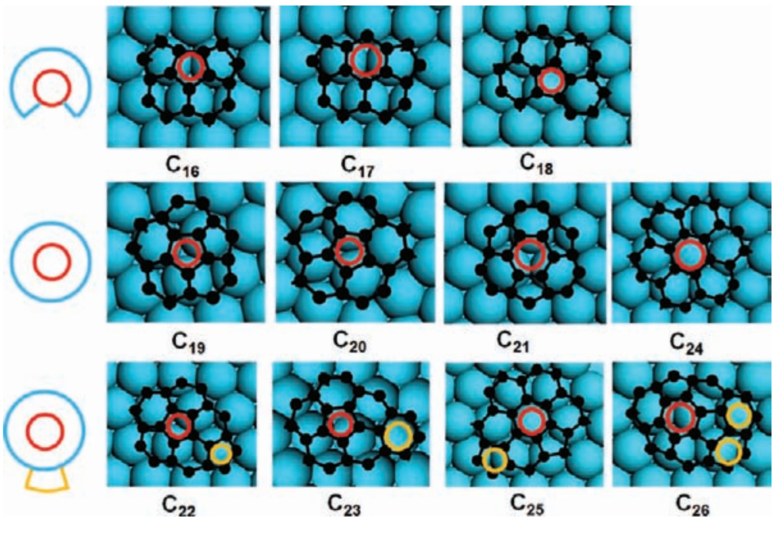

Figure 4. Ground-state structures of C_{16}−C_{26} on Rh(111) surface. They can be classified into three groups: C_{16}−C_{18} have unclosed core−shell (**CS−**) structures; C_{19}−C_{21} and C_{24} are closed core−shell structures (**CS**); and C_{22}, C_{23}, C_{25}, and C_{26} have a core−shell geometry with one or two additional rings (**CS+**).

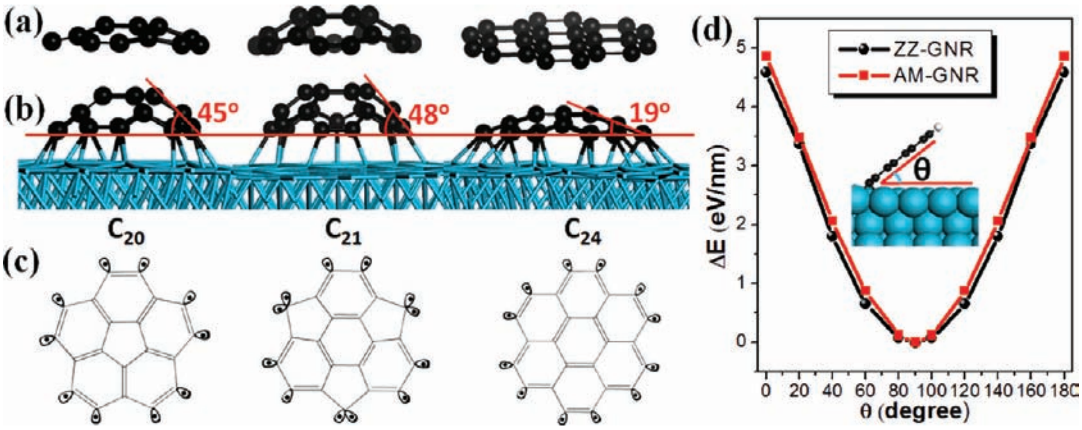

Figure 5. (a) Free-standing and (b) Rh(111) surface-supported C_{20}, C_{21}, and C_{24} clusters. (c) Illustration of their reactive sites. (d) Energetic preference of upright standing graphene nanoribbon (GNR) on Rh(111) surface. GNRs with both armchair (AC-GNRs) and zigzag (ZZ-GNRs) edges are calculated; computational details can be found in Supporting Information.

Table 1. Characteristics of C_{20}, C_{21}, and C_{24} on Rh(111) Surface[a]

	C_{20}	C_{21}	C_{24}
symmetry of free C_N	C_{5v}	C_{3v}	C_{6v}
symmetry of C_N@Rh(111)	C_s	C_{3v}	C_3
number of edge atoms	10	9	12
number of reactive sites	10	12	12
tilt angle at the edge, θ (deg)	45	48	19
E_{ad} of C_N on Rh (111) (eV)	12.5 (12.5)	17.1 (16.5)	14.3 (13.9)
formation energy of free C_N clusters (eV)	22.41	26.40	24.90

[a] The adsorption energy of C_N@Rh(111) is defined as $E_{ad} = [E(C_N) + E(Rh) - E(C_N@Rh)]$, where $E(C_N)$, E(Rh), and $E(C_N@Rh)$ are the total energies of free C_N cluster, Rh substrate, and Rh-supported C_N, respectively. Values of E_{ad} shown in parentheses were calculated with the spin-polarized DFT method.

Both theoretical analysis and comparison with experimental measurements, including STM images, d*I*/d*V* curves, and cluster heights, confirm that C_{21} is the experimentally observed dominating C cluster in graphene CVD growth on Rh(111) or Ru(0001) surface. The same magic size effect is also shown in C_N@Ni(111)[19] and C_N@Cu(111) curves (Figure 1a,b and Figures S2 and S3 in Supporting Information). Although we do not have enough evidence to conclude that the core−shell structured *C_{21} cluster is a universal magic cluster on all metal surfaces*, the striking result implies the uniqueness of the C_{21} cluster on most transition metal surfaces.

To understand the high stability of C_{21} on transition metal surfaces, using Rh(111) surface as an example, we applied a systematic analysis from the aspects of symmetry, geometry, and electronic structure. Similar analysis can be applied to C clusters on other metal surfaces as well.

First, as shown in Figure 4, the ground-state structures of C_N@Rh(111) can be classified into three groups: (i) small clusters (C_{16}, C_{17}, and C_{18}) have a unclosed core−shell geometry (denoted as **CS−**); (ii) medium-sized clusters (C_{19}, C_{20}, and C_{21}) and C_{24} have a closed core−shell formation (denoted as **CS**); (iii) large clusters (C_{22}, C_{23}, C_{25}, and C_{26}) have a core−shell structure with one or two additional rings (denoted as **CS+**). Very similar classification can be applied to C_N on other three metal surfaces (see Figure S2 in Supporting Information). It has been established that clusters with a closed core−shell geometry are generally more stable than those unclosed or with additional atoms.[36,37] Hence, it is not surprising that both magic clusters, C_{21} and C_{24}, have the **CS** geometry.

Among the four **CS** clusters, C_{19} and C_{20} have a pentagonal core, while the core of C_{21} and C_{24} is a hexagon. Among them, the C_{19} has the lowest C_s symmetry. In contrast, the free-standing clusters C_{20}, C_{21}, and C_{24} have very high C_{5v}, C_{3v}, and C_{6v} symmetries, respectively (Figure 5a). Upon binding to the Rh(111) surface, which has a C_{3v} symmetry, the symmetries of the supported C_{20} and C_{24} are reduced to C_s and C_3, respectively, but C_{21} is able to maintain its C_{3v} symmetry. The high symmetry allows C_{21} to achieve strong binding between all its edge atoms and the metal surface and thus enhances its stability.

In order to further understand the uniqueness of the supported C_{21} cluster with regard to C_{20} and C_{24}, a comparison of their characteristics is presented in Table 1 and Figure 5. These free-standing clusters show very different characteristics from their metal−supported counterparts. With three pentagons incorporated, the C_{21} is highly curved; C_{20} is slightly curved because of the pentagon core. In sharp contrast, the 7-6MRs C_{24} is completely flat.

Anchoring on the metal surface (Figure 5b), all three clusters tend to form a domelike geometry. That is attributed to the fact that *a graphene edge tends to stand upright on the metal surface*. As shown in Figure 5d, a vertically standing graphene has minimum edge formation energy. The energy tendency shows that nanographene prefers a domelike shape to minimize its edge formation energy.[9] As shown in Figure 5b, C_{21} has the greatest tilt angle of 48° at the edge, and the 7-6MRs C_{24} has the least tilt angle of 19°. Such a difference results in a notable adsorption energy difference of ~2.0 eV/nm or ~0.5 eV/edge atom. Moreover, the peculiar electronic structure of the three pentagons of C_{21} is also beneficial for strong binding between the cluster and metal surface. Although C_{21} has the smallest number of edge atoms (i.e., 10, 9, and 12 for C_{20}, C_{21}, and C_{24}, respectively), every edge atom of a pentagon has two active unpaired electrons to interact with the metal surface or two reactive sites (Figure 5c). So, in C_{21}, the effective number of reactive sites is actually greater than the number of its edge atoms, and therefore the interaction between C_{21} and metal surface is significantly enhanced. As shown in

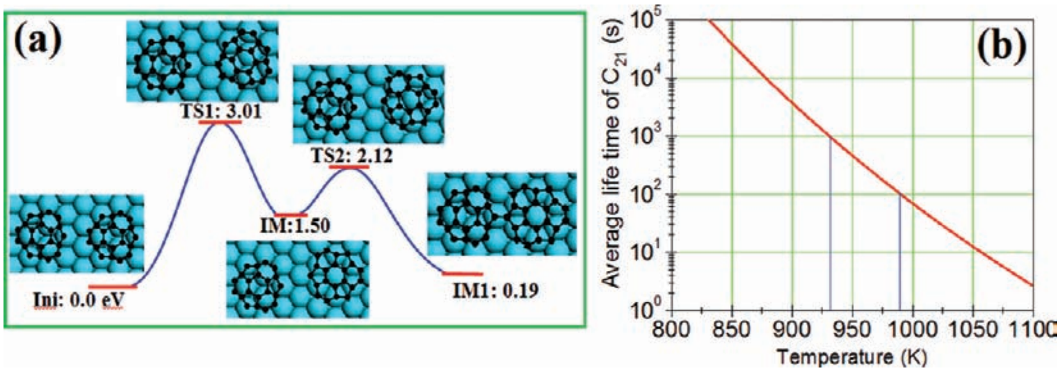

Figure 6. (a) Kinetic process of dimerization of two C_{21} clusters on Rh(111) surfaces. (b) Calculated average lifetime of C_{21} on Rh(111) surface.

Table 1, the total adsorption energy of C_{21} on Rh(111) surface is 17.1 eV, which is about 20% greater than that of C_{24}, 14.3 eV. So although the free-standing C_{21} has higher formation energy than C_{24}, the difference has been greatly compensated by the stronger edge−metal interaction.

From the above analysis, we can conclude that the uniqueness of the C_{21} cluster on metal surface is attributed to

(i) its closed core−shell geometry;
(ii) its high symmetry;
(iii) the strong binding between pentagon edges and the metal surface;
(iv) the tendency of upright standing graphene edge on metal surface.

Points i−iii are characteristics of the C_{3v} C_{21} cluster. As shown in Figure S4 of Supporting Information, point iv, the tendency of upright standing graphene edge, is valid for all four explored metal surfaces. As shown in recent research, it is also valid for graphene on diamond surface.[38] Therefore, we anticipate C_{21} to be an universal magic cluster on most transition metal surfaces. Due to the limitation of computational resources, we explored only four selected metal surfaces and all of them support the prediction. Certainly more extensive calculations are needed in the future.

The uniqueness of C_{21} makes it the most stable C cluster on metal surface. But, as a small graphene island with significant edge energy penalty, it cannot be more stable than very large ones, and thus their aggregation or coalescence must happen at a later stage of graphene growth.[9] So the dominating C_{21} as C precursor in the initial graphene CVD growth must be a *kinetic behavior*. The kinetic stability of C_{21} clusters at elevated temperature requires a large barrier to prevent their aggregation or maintain them to survive a macroscopic lifetime (e.g., in minutes). The barrier of aggregation from two independent C_{21} clusters to a C_{21} dimer is calculated and shown in Figure 6a. The highest energy barrier, E^*, during dimerization of two C_{21} clusters was found to be 3.01 eV. This notable high energy barrier prevents C_{21} clusters from forming C_{21} dimers.

As shown in Figure 6b, the average lifetime of C_{21} [which is estimated by $\tau = (h/k_BT)\exp(E^*/k_BT)$, where k_B and h are Boltzmann and Planck constants, respectively] is 100−1000 s in the temperature range 930−985 K. Experimentally, the aggregation of dominating C clusters into large graphene islands or the initiation of graphene growth on Rh(111) occurs at ~870 K.[25] Similarly, the aggregation of uniformed C clusters on Ru(0001) and Ir(111) surfaces occurs at a similar temperature range, that is, 1000−1100 and 970 K, respectively.[10,26] This agreement between the theoretical prediction and experimental observations further confirms the validity of our conclusion.

4. CONCLUSIONS

In conclusion, the most stable structures of C_N (N = 16, ..., 26) on four selected metal surfaces [Rh(111), Ru(0001), Ni(111), and Cu(111)] are explored by ab initio methods. The C_{21} cluster, with C_{3v} symmetry and three isolated pentagons, possesses superior stability due to its closed core−shell structure, high symmetry, and strong binding to the metal substrate. Comparisons between the simulated STM images and experimental ones, experimental dI/dV curves and calculated LDOS, and measured cluster height and the height of optimized clusters all confirm that C_{21} is the observed dominating C precursor in graphene CVD growth on Rh(111) and Ru(0001) surfaces. Because the lack of direct experimental measurement of the cluster's atomic structure, one might argue that none of these lines of evidence is 100% reliable. But it is hard to believe that all these agreements and the result of ab initio calculations are coincidences.

One may argue that these 5-membered rings may lead to caplike graphene islands instead of flat ones. But, as C21 is a quite small island, the flatness of CVD graphene can be achieved by the addition of 7-membered rings at the later stage. In this case, the present work is helpful to understand two puzzling experimental observations: (1) the observation of grain boundary loops in graphene[39,40] and (2) the fact that the domains of epitaxial graphene always contain a disordered region related to their nucleation point.[1]

The present study shows that it is potentially possible to synthesize uniform C_{21} graphene quantum dots on various metal surfaces at elevated temperatures. On the other hand, the simultaneous fusion of less mobile, high-coverage C_{21} clusters on a metal surface must result in highly concentrated nuclei or graphene islands on the metal surface,[25−27] and the coalescence of these islands will inevitably lead to the formation of graphene grain boundary and thus the quality of the synthesized graphene must be low.[41,42] Thus, experimentally, avoiding the formation of uniform magic C clusters on metal surface is crucial for achieving high-quality graphene synthesis.

■ ASSOCIATED CONTENT

Ⓢ Supporting Information. Four figures, showing formation of various isomers of C_{21}@Rh(111); ground-state structures of C_N (N = 16−24) clusters on Rh(111), Ru(0001), Ni(111), and Cu(111); simulated STM images of C_{21} and C_{24} clusters on Ru(0001), Ni(111), and Cu(111) surfaces; and preference of upright standing graphene formation on selected metal surfaces.

This material is available free of charge via the Internet at http://pubs.acs.org.

AUTHOR INFORMATION

Corresponding Author

tcfding@inet.polyu.edu.hk; zhaojj@dlut.edu.cn; xschen@mail.sitp.ac.cn

Author Contributions

‖These authors contributed equally to this study

ACKNOWLEDGMENT

We appreciate the inspiring suggestion on the chemistry of C_{21} by Professor Z. Y. Lin of HKUST and the fruitful discussion with Professor W. X. Li of Dalian Institute of Chemical Physics. The research in Hong Kong PolyU was supported by Hong Kong research grants (B-Q26K; A-PK89). The research at Shanghai Institute for Technical Physics was supported by the National Natural Science Foundation of China, Grants 10725418, 10734090, and 10990104. Computational resources from the Shanghai Supercomputer Center are acknowledged.

REFERENCES

(1) Wu, W.; Jauregui, L. A.; Su, Z.; Liu, Z.; Bao, J.; Chen, Y. P.; Yu, Q. *Adv. Mater.* **2011**, *23*, 4898–4903.

(2) Dimiev, A.; Kosynkin, D. V.; Sinitskii, A.; Slesarev, A.; Sun, Z.; Tour, J. M. *Science* **2011**, *331*, 1168–1172.

(3) Liu, Z.; Song, L.; Zhao, S.; Huang, J.; Ma, L.; Zhang, J.; Lou, J.; Ajayan, P. M. *Nano Lett.* **2011**, *11*, 2032–2037.

(4) Ci, L.; Song, L.; Jin, C.; Jariwala, D.; Wu, D.; Li, Y.; Srivastava, A.; Wang, Z. F.; Storr, K.; Balicas, L.; Liu, F.; Ajayan, P. M. *Nat. Mater.* **2010**, *9*, 430–435.

(5) Wintterlin, J.; Bocquet, M. L. *Surf. Sci.* **2009**, *603*, 1841–1852.

(6) Starodub, E.; Maier, S.; Stass, I.; Bartelt, N. C.; Feibelman, P. J.; Salmeron, M.; McCarty, K. F. *Phys. Rev. B* **2009**, *80*, No. 235422.

(7) Marchini, S.; Günther, S.; Wintterlin, J. *Phys. Rev. B* **2007**, *76*, No. 075429.

(8) Preobrajenski, A. B.; Ng, M. L.; Vinogradov, A. S.; Mårtensson, N. *Phys. Rev. B* **2008**, *78*, No. 073401.

(9) Lacovig, P.; Pozzo, M.; Alfè, D.; Vilmercati, P.; Baraldi, A.; Lizzit, S. *Phys. Rev. Lett.* **2009**, *103*, No. 166101.

(10) Coraux, J.; N'Diaye, A. T.; Engler, M.; Busse, C.; Wall, D.; Buckanie, N.; Heringdorf, F.-J. M. z.; van Gastel, R.; Poelsema, B.; Michely, T. *New J. Phys.* **2009**, *11*, No. 023006.

(11) Zhang, Y.; Gomez, L.; Ishikawa, F. N.; Madaria, A.; Ryu, K.; Wang, C.; Badmaev, A.; Zhou, C. *J. Phys. Chem. Lett.* **2010**, *1*, 3101–3107.

(12) Lee, Y.; Bae, S.; Jang, H.; Jang, S.; Zhu, S.-E.; Sim, S. H.; Song, Y. I.; Hong, B. H.; Ahn, J.-H. *Nano Lett.* **2010**, *10*, 490–493.

(13) Sutter, P.; Sadowski, J. T.; Sutter, E. *Phys. Rev. B* **2009**, *80*, No. 245411.

(14) Land, T. A.; Michely, T.; Behm, R. J.; Hemminger, J. C.; Comsa, G. *Surf. Sci.* **1992**, *264*, 261–270.

(15) Kwon, S.-Y.; Ciobanu, C. V.; Petrova, V.; Shenoy, V. B.; Bareño, J.; Gambin, V.; Petrov, I.; Kodambaka, S. *Nano Lett.* **2009**, *9*, 3985–3990.

(16) Gao, L.; Guest, J. R.; Guisinger, N. P. *Nano Lett.* **2010**, *10*, 3512–3516.

(17) Li, X.; Cai, W.; An, J.; Kim, S.; Nah, J.; Yang, D.; Piner, R.; Velamakanni, A.; Jung, I.; Tutuc, E.; Banerjee, S. K.; Colombo, L.; Ruoff, R. S. *Science* **2009**, *324*, 1312–1314.

(18) Amara, H.; Bichara, C.; Ducastelle, F. *Phys. Rev. B* **2006**, *73*, No. 113404.

(19) Gao, J.; Yip, J.; Zhao, J.; Yakobson, B. I.; Ding, F. *J. Am. Chem. Soc.* **2011**, *133*, 5009–5015.

(20) Saadi, S.; Abild-Pedersen, F.; Helveg, S.; Sehested, J.; Hinnemann, B.; Appel, C. C.; Nørskov, J. K. T. *J. Phys. Chem. C* **2010**, *114*, 11221–11227.

(21) Wu, P. *J. Chem. Phys.* **2010**, *133*, No. 071101.

(22) van Wesep, R. G.; Chen, H.; Zhu, W.; Zhang, Z. *J. Chem. Phys.* **2011**, *134*, No. 171105.

(23) Cheng, D.; Barcaro, G.; Charlier, J.-C.; Hou, M.; Fortunelli, A. *J. Phys. Chem. C* **2011**, *115*, 10537–10543.

(24) Gao, J.; Yuan, Q.; Hu, H.; Zhao, J.; Ding, F. *J. Phys. Chem. C* **2011**, *115*, 17695–17703.

(25) Wang, B.; Ma, X.; Caffio, M.; Schaub, R.; Li, W.-X. *Nano Lett.* **2011**, *11*, 424–430.

(26) Cui, Y.; Fu, Q.; Zhang, H.; Bao, X. *Chem. Commun.* **2011**, *47*, 1470–1472.

(27) Lu, J.; Yeo, P. S. E.; Gan, C. K.; Wu, P.; Loh, K. P. *Nat. Nanotechnol.* **2011**, *6*, 247–252.

(28) Kresse, G.; Furthmüller, J. *Comput. Mater. Sci.* **1996**, *6*, 15–50.

(29) Kresse, G.; Furthmüller, J. *Phys. Rev. B* **1996**, *54*, 11169–11186.

(30) Blöchl, P. E. *Phys. Rev. B* **1994**, *50*, 17953–17979.

(31) Perdew, J. P.; Burke, K.; Ernzerhof, M. *Phys. Rev. Lett.* **1996**, *77*, 3865–3868.

(32) Mills, G.; Jónsson, H.; Schenter, G. K. *Surf. Sci.* **1995**, *324*, 305–337.

(33) Tersoff, J.; Hamann, D. R. *Phys. Rev. Lett.* **1983**, *50*, 1998–2001.

(34) Baletto, F.; Ferrando, R. *Rev. Mod. Phys.* **2005**, *77*, 371–423.

(35) Chen, H.; Zhu, W.; Zhang, Z. *Phys. Rev. Lett.* **2010**, *104*, No. 186101.

(36) Šiber, A. *Phys. Rev. B* **2004**, *70*, No. 075407.

(37) Tai, T. B.; Grant, D. J.; Nguyen, M. T.; Dixon, D. A. *J. Phys. Chem. A* **2009**, *114*, 994–1007.

(38) Yuan, Q.; Hu, H.; Gao, J.; Ding, F.; Liu, Z.; Yakobson, B. I. *J. Am. Chem. Soc.* **2011**, *133*, 16072–16079.

(39) Cockayne, E.; Rutter, G. M.; Guisinger, N. P.; Crain, J. N.; First, P. N.; Stroscio, J. A. *Phys. Rev. B* **2011**, *83*, No. 195425.

(40) Meyer, J. C.; Kurasch, S.; Park, H. J.; Skakalova, V.; Künzel, D.; Groß, A.; Chuvilin, A.; Algara-Siller, G.; Roth, S.; Iwasaki, T.; Starke, U.; Smet, J. H.; Kaiser, U. *Nat. Mater.* **2011**, *10*, 209–215.

(41) Yakobson, B. I.; Ding, F. *ACS Nano* **2011**, *5*, 1569–1574.

(42) Yu, Q.; Jauregui, L. A.; Wu, W.; Colby, R.; Tian, J.; Su, Z.; Cao, H.; Liu, Z.; Pandey, D.; Wei, D.; Chung, T. F.; Peng, P.; Guisinger, N. P.; Stach, E. A.; Bao, J.; Pei, S.-S.; Chen, Y. P. *Nat. Mater.* **2011**, *10*, 443–449.